OPTICS

# A three-dimensional photonic topological insulator using a two-dimensional ring resonator lattice with a synthetic frequency dimension

Qian Lin[1], Xiao-Qi Sun[2], Meng Xiao[3], Shou-Cheng Zhang[2], Shanhui Fan[3,4]*



**In the development of topological photonics, achieving three-dimensional topological insulators is of notable interest since it enables the exploration of new topological physics with photons and promises novel photonic devices that are robust against disorders in three dimensions. Previous theoretical proposals toward three-dimensional topological insulators use complex geometries that are challenging to implement. On the basis of the concept of synthetic dimension, we show that a two-dimensional array of ring resonators, which was previously demonstrated to exhibit a two-dimensional topological insulator phase, automatically becomes a three-dimensional topological insulator when the frequency dimension is taken into account. Moreover, by modulating a few of the resonators, a screw dislocation along the frequency axis can be created, which provides robust one-way transport of photons along the frequency axis. Demonstrating the physics of screw dislocation in a topological system has been a substantial challenge in solid-state systems. Our work indicates that the physics of three-dimensional topological insulators can be explored in standard integrated photonic platforms, leading to opportunities for novel devices that control the frequency of light.**

## INTRODUCTION

The discovery of two-dimensional (2D) topological photonic systems expands the scope of topological materials from fermions to bosons and enables new ways for controlling the propagation of electromagnetic waves (*1*–*13*). A natural next step is the experimental realization of photonic 3D topological insulators (*14*, *15*). However, existing proposals (*16*, *17*) to realize 3D photonic topological insulators require complex geometries. Here, we propose to explore such 3D topological physics using a 2D array of ring resonators, which is directly implementable in a standard integrated photonic platform. A wide variety of topological phases can be created using 2D arrays of ring resonators (*4*, *5*, *9*, *10*). Moreover, since a ring supports a discrete set of resonant modes forming a frequency comb (*18*–*21*), one can consider a ring to have a synthetic dimension along the frequency axis. As a result, a 2D array of ring resonators that behaves like a 2D topological insulator near the resonant frequency of a single ring will naturally become a 3D topological insulator when the additional synthetic dimension is considered. The 3D topological order in this system can be revealed by modulating the rings. For example, by modulating a few resonators in the array, a screw dislocation parallel to the frequency axis can be created, which supports topologically protected one-way transport (*22*) along the frequency axis and serves as a spectral probe for the 3D topological order in our proposed system.

3D topological insulators are characterized by four indices (*23*): a scalar $\nu_0$ and a triad ($\nu_1$, $\nu_2$, $\nu_3$) that defines a reciprocal lattice vector $\mathbf{G}_\nu$. $\nu_0$ classifies 3D topological insulators into two general classes: weak and strong. The strong class has $\nu_0 \neq 0$, and gapless surface states exist on any 2D surface of the sample. On the other hand, weak topological insulators have $\nu_0 = 0$ but $\mathbf{G}_\nu \neq 0$. Since $\mathbf{G}_\nu$, which characterizes the topology of a weak topological insulator, depends on crystal orientation, the existence of gapless surface states in a weak topological insulator also depends on the orientation of the surface. Originally assumed to be less robust than their strong counterpart, weak 3D topological insulators have been recently shown to have rich physics and unexpectedly strong protection against disorders (*24*). In theory, weak topological insulators can be realized by simply stacking multiple layers of 2D topological insulators. However, in typical electronic or photonic systems, when stacking multiple layers together in real space, it is difficult to control the interlayer coupling such that the 2D topological gap, which is usually very small, is still preserved in 3D. Here, we show that a 2D array of ring resonators with a synthetic frequency dimension naturally realizes a weak 3D topological insulator with minimal interlayer coupling, providing a clean and versatile platform to study the physics of 3D topological insulators.

Our system is ideal for studying screw dislocations in 3D topological insulators, which represents the interaction of two types of topology: the topology of band structures in reciprocal space and the topology of lattices in real space. It has been predicted that a dislocation line in a 3D topological insulator traps an integer number of 1D topologically protected states (*22*). However, observing this effect in a condensed matter system is extremely difficult because creating a single dislocation line in solid-state materials is technically challenging and energetically unfavorable (*25*). Our photonic system based on the synthetic dimension provides an experimentally feasible way to controllably realize a single dislocation in a 3D topological insulator using dynamic modulation and to observe the topologically protected states. Moreover, unlike previous studies of topological photonics in the synthetic dimension (*18*, *19*, *21*) that requires modulating a large number of optical elements, here the dislocation is implemented with only a few modulated rings. Thus, our proposal presents a great opportunity to harness the benefits of topological photonics in the synthetic frequency dimension, to achieve useful effects such as robust one-way frequency conversions, for experiments and future applications.

[1]Department of Applied Physics, Stanford University, Stanford, CA 94305, USA. [2]Department of Physics, Stanford University, Stanford, CA 94305, USA. [3]Ginzton Laboratory, Stanford University, Stanford, CA 94305, USA. [4]Department of Electrical Engineering, Stanford University, Stanford, CA 94305, USA.
*Corresponding author. Email: shanhui@stanford.edu

## RESULTS AND DISCUSSION

### Constructing a 3D topological insulator

We start by constructing an array of ring resonators that supports 2D topological states. As an example, we use a 2D array that exhibits the

quantum spin Hall effect (QSHE) (*4*), although the results generalize to all ring array configurations supporting photonic topological states (*5*, *9*, *20*). Consider a generic tight-binding Hamiltonian describing the QSHE on a square lattice

$$H^{2D} = -t \sum_{x,y,\sigma} \left( a^{\dagger}_{x+1,y,\sigma} a_{x,y,\sigma} + e^{i\sigma x\phi} a^{\dagger}_{x,y+1,\sigma} a_{x,y,\sigma} + h.c. \right) \quad (1)$$

where $t$ is the strength of nearest-neighbor coupling, $(x, y)$ labels the lattice sites, $\sigma = \pm 1$ represent two pseudospins, and *h. c.* is short for Hermitian conjugate. In this Hamiltonian, the two pseudospins are decoupled. A particle with $\sigma = +1$ spin sees a directional phase of $+ x\phi$ ($-x\phi$) when hopping up (down) along the $y$ direction. This corresponds to a uniform magnetic flux of $\phi$ in each unit cell. A particle with $\sigma = -1$ spin sees the opposite directional coupling phase and thus a uniform magnetic flux of $-\phi$ per unit cell. Therefore, this Hamiltonian describes a boson subject to a pseudospin-dependent out-of-plane uniform magnetic field and exhibits the QSHE.

The photonic structure that implements this Hamiltonian consists of a square lattice of identical site rings coupled to their nearest neighbors through identical link rings (*4*), as shown in Fig. 1B. Here, the $(x, y)$ labels in Eq. 1 are pairs of half-integers representing the centers of site rings, with the origin of the coordinate system defined at the center of the array. The circumferences of the rings are chosen such that the resonance of the site rings matches the antiresonance of the link rings, and photons are strongly confined in the site rings. The resulting photonic band structure near the resonance of the site ring can be well captured by a tight-binding model. In the absence of backscattering in the waveguides forming the rings, the clockwise and counterclockwise propagating modes in the site ring, representing the two spins in the QSHE, are degenerate and decoupled. To obtain a pseudospin-dependent effective magnetic field for photons, the centers of the $y$-coupling link rings are shifted away from the line segments that connect the center of two adjacent site rings. As a result, the left and right branches of a link ring differ in length. When a photon in the clockwise mode of a site ring hops to the adjacent site ring in the negative $y$ direction, it acquires a smaller phase than that when it hops in the positive $y$ direction. Thus, the photon acquires direction-dependent hopping phase proportional to the amount of shift of the link ring. The shifts of the link rings vary from one column of the array to the next to provide the $\pm x\phi$ directional coupling phase in the QSHE Hamiltonian in Eq. 1.

We confirm the existence of the 2D topological bandgap in this array of ring resonators by computing the topological edge states on a stripe of the array that is finite in the $x$ direction and infinite in the $y$ direction. The shifts of the link rings are chosen to produce a uniform magnetic field of 1/3 flux quanta through each square unit cell. We model our system using the transfer-matrix method (see the Supplementary Materials) (*9*), which is more accurate than the tight-binding model, because it accounts for the different waveguide modal amplitudes in different parts of a ring. We numerically solve for the eigenfrequencies and eigenstates of the transfer-matrix model for the clockwise mode in the site rings, and the results are plotted in Fig. 2. The band structure shown in Fig. 2A exhibits three magnetic bands near the resonant frequency of the site rings and a large bandgap for a frequency detuning from the resonance $\delta\omega$ between 0 and $-0.08\ \Omega$. A pair of edge states with opposite propagation directions span the bandgap, and their eigenstate wave functions are localized on opposite edges of the stripe, as shown in Fig. 2 (B and C).

The microring array discussed above exhibits a quantum spin Hall (QSH) phase for photons near a resonant frequency $\omega_0$ of the site ring. Since each site ring supports multiple resonances with different resonant frequencies separated by the free spectral range of the ring $\Omega \ll \omega_0$, if we take into account the frequency dimension, the system then

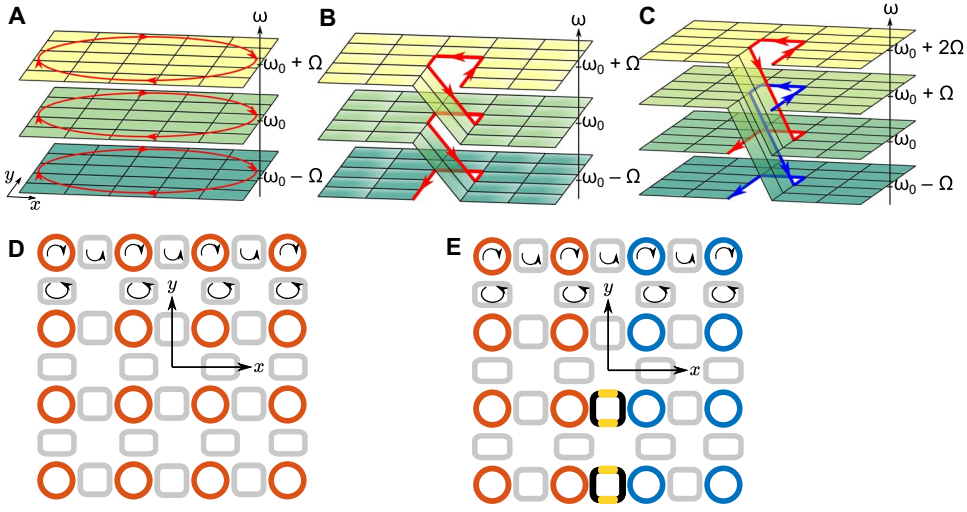


**Fig. 1. 3D topological insulator and screw dislocation.** (**A**) 3D lattice formed by stacking layers of 2D QSH states. The set of discrete resonances of a ring forms a lattice in the synthetic frequency dimension. (**B**) Microring array implementing (A). Orange and gray rings are site and link rings with the same free spectral range $\Omega$. The link rings providing coupling along the $y$ direction are spatially shifted along the $x$ direction to provide directional coupling phases that implement the Landau gauge. (**C** and **D**) Screw dislocations with Burgers vectors **B** = (0, 0, −1) and **B** = (0, 0, −2), respectively. One-way topological states spatially localized around the dislocation flow along the synthetic frequency dimension. (**E**) Microring array implementing (C) and (D). Orange and blue rings are site rings with the same resonant frequency but different resonant wave vectors. Gray rings are static link rings providing intralayer couplings. Black rings are dynamic link rings whose refractive index is modulated at a frequency equal to the free spectral range $\Omega$. They couple a resonant mode at frequency $\omega_0$ in the blue ring to a resonant mode at frequency $\omega_0 + \Omega$ in the orange ring, forming the interlayer links shown in (C) and (D).

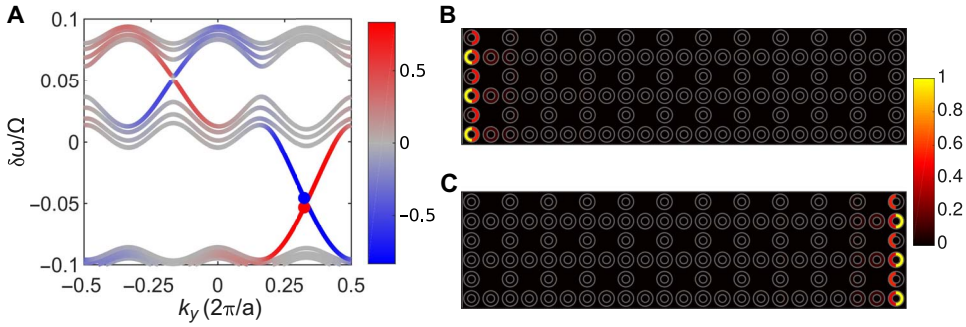


**Fig. 2. 2D QSHE in a microring array.** (**A**) Band structure and (**B** and **C**) edge states of a 2D stripe of rings with an effective magnetic flux of 1/3 flux quanta per unit cell for the clockwise mode in the site rings. The stripe is infinite along the *y* direction and has 12 site rings along the *x* direction. In (A), the color scale for the band structure represents the difference of eigenstate modal intensity between the rings on the left and right edges of the structure. Thus, the orange and blue lines are edge states localized on the left and right edges of the stripe, respectively. The orange and blue dots represent the states plotted in (B) and (C), respectively. (B and C) Modal intensities in the rings for the two edge states, shown for three periods along the *y* direction. The scattering amplitude at each site ring to the link ring coupler is $\gamma_s = 0.75$.

corresponds to layers of decoupled 2D QSH states, each associated with a resonance of the site ring. The tight-binding Hamiltonian describing this system is

$$H^{3D} = \sum_m \Big[ \omega_m \sum_{x,y,\sigma} a^\dagger_{x,y,m,\sigma} a_{x,y,m,\sigma} - t \sum_{x,y,\sigma} \left( a^\dagger_{x+1,y,m,\sigma} a_{x,y,m,\sigma} + e^{i\sigma x\phi} a^\dagger_{x,y+1,m,\sigma} a_{x,y,m,\sigma} + h.c. \right) \Big] \quad (2)$$

where $a^\dagger_{x,y,m,\sigma}$ ($a_{x,y,m,\sigma}$) is the creation (annihilation) operator for the *m*th-order resonant mode of the site ring centered at (*x*, *y*). To show explicitly that Eq. 2 represents the stacking of layers of 2D QSH states, we define $c_{x,y,m,\sigma} = a^{-i\omega_m t} a_{x,y,m,\sigma}$ and transform Eq. 2 into the rotating frame

$$H^{3D} = -t \sum_{m,x,y,\sigma} \left( c^\dagger_{x+1,y,m,\sigma} c_{x,y,m,\sigma} + e^{i\sigma x\phi} c^\dagger_{x,y+1,m,\sigma} c_{x,y,m,\sigma} + h.c. \right) \quad (3)$$

Equation 3 describes a 3D system indexed by (*x*, *y*, *m*), which consists of layers of 2D QSH states stacked along the frequency axis labeled by *m* with no interlayer couplings. The 3D system is gapped since the 2D magnetic bandgaps shown in Fig. 2A are preserved. The reciprocal space of this 3D lattice is labeled by the wave vectors $k_x$ and $k_y$ along the two spatial dimensions and the wave vector $k_f$ along the synthetic frequency dimension.

The triad of weak topological indices of such a system is (*23*, *26*)

$$\nu_1 = C^{yz}(k_x) = 0, \quad \nu_2 = C^{zx}(k_y) = 0, \quad \nu_3 = C^{xy}(k_z) = C^{2D} \quad (4)$$

where $\nu_3 = C^{xy}(k_z)$ is a first Chern number for the 3D topological insulator and is defined as the integral of the Berry curvature $\mathcal{F}_{xy}(\mathbf{k})$ in the $k_x - k_y$ momentum plane within the first Brillouin zone. $\nu_1$ and $\nu_2$ are similarly defined.

The result in Eq. 4 can be understood as follows. With no interlayer coupling, the Fourier transform of the Hamiltonian in Eq. 3 is $k_z$ independent. Consequently, the Berry curvature $\mathcal{F}_{yz}(\mathbf{k}) = \mathcal{F}_{zx}(\mathbf{k}) = 0$ for all wave vectors $\mathbf{k}$, and the first two indices vanish. The third index $C^{xy}(k_z)$ is identical to the 2D QSH Chern number $C^{2D}$ in Eq. 1. For an effective magnetic field of + 1/3 (−1/3) flux quanta per unit cell for the + (−) spin, $C^{2D} = \pm 1$ ($\mp 1$) for the lower-frequency and higher-frequency magnetic bandgaps shown in Fig. 2A, respectively (*27*, *28*). Since the band structure of the bulk is completely gapped, $C^{xy}(k_z)$ cannot change as a function of $k_z$. The same applies to the other two indices.

## Screw dislocation and robust one-way frequency conversion

To probe the topological states in a weak topological insulator, one needs to break its crystal symmetry by cutting a surface or introducing a dislocation. In our system, in the absence of dynamic modulation, there is a complete lack of interlayer coupling since the frequency does not change. Such a lack of coupling provides an ideal weak 3D TI with a large topological bandgap in the bulk. However, it also means that any measurable surface topological signature is intrinsically 2D. To demonstrate a genuinely 3D signature of the topological phase, we propose to modulate a few rings in the array to introduce a single screw dislocation line into our 3D TI. It has been predicted that a single dislocation line in a 3D TI can trap 1D topologically protected modes (*22*, *26*, *29*, *30*). For a 3D TI characterized by $\mathbf{G}_\nu$ (*23*), the number of 1D topologically protected modes trapped by a dislocation with a Burgers vector $\mathbf{B}$ is $\mathbf{G}_\nu \cdot \mathbf{B}/2\pi$. In contrast to previous studies of screw dislocations that mostly focused on their signature in scattering of electrons in the far field (*31*–*33*), in our system, one can isolate and probe a single dislocation line and demonstrate its interaction with the topology of photonic bands.

To introduce a screw dislocation as shown in Fig. 1C, we replace a few in-plane coupling terms in Eq. 3 with interlayer coupling terms

$$c^\dagger_{x+1,y,m,\sigma} c_{x,y,m,\sigma} + h.c. \rightarrow c^\dagger_{x+1,y,m-1,\sigma} c_{x,y,m,\sigma} + h.c.,$$
$$\forall x = -0.5, \quad y < 0 \quad (5)$$

This introduces a branch cut at $x = 0$, $y < 0$. Away from this branch cut, the Hamiltonian is unchanged from Eq. 3. Across the branch cut, tunneling toward +*x* (−*x*) is associated with moving down (up) one layer along the frequency dimension. This represents a screw dislocation located at (0, 0).

A microring array that implements a screw dislocation in the above-mentioned 3D TI is shown in Fig. 1E. The structure is similar to Fig. 1B, which exhibits a 2D QSH phase. In particular, all the rings have the same free spectral range Ω, and all the site rings have the same resonant frequency, which coincides with the antiresonance of the static link

rings. The differences from the 2D QSH configuration are as follows: (i) The waveguide forming the site rings at $x > 0$ (blue) and $x < 0$ (orange) has different wave vectors for the same resonant frequency. This can be achieved in the waveguides if the blue and orange site rings have different refractive indices or cross-section dimensions. (ii) We replace the static link rings (gray) on the branch cut with dynamic link rings (black). The details of one of these modified link rings are provided in Fig. 3A and in the Supplementary Materials. A dynamic link ring is formed by a slot waveguide that supports an even mode and an odd mode. Direct photonic transition between these two modes is induced by dynamically modulating the refractive index of the waveguide at the frequency Ω, which is equal to the free spectral range of the rings (*34*, *35*). Outside of the modulation region, the air gap in the slot waveguide is tapered down so that the wave vectors of the even and odd modes differ. The odd mode is phase matched to the orange site rings, while the even mode is phase matched to the blue site rings. The phase-mismatched couplings are minimized. Consequently, the dynamic link ring couples the *m*th resonant modes in the blue ring to the $(m + 1)$th resonant modes in the orange ring (Fig. 3B). Hopping counterclockwise around a closed path encircling the center of the array in Fig. 1E decreases the frequency by Ω. Thus, a screw dislocation with a Burgers vector $\mathbf{B} = (0, 0, -1)$ is created at the center of the array. Practical design considerations for the rings and an example are provided in the Supplementary Materials.

Consider a 12 × 12 array of microrings with a screw dislocation at the center. We assume that the resonant modes extend infinitely along the frequency axis and use periodic boundary conditions along the *x* and *y* directions. The resulting spectrum for the clockwise mode as a function of the wave vector $k_f$ along the dislocation line is plotted in Fig. 4A. The three groups of bulk bands (gray lines) and the topological bandgap can be clearly distinguished and have a frequency range similar to that of the 2D QHE state shown in Fig. 2A. The dislocation line at (0, 0) supports a mode that spans the topological bandgap and propagates unidirectionally down the frequency axis, as shown by the red line in Fig. 4A. The corresponding eigenstate wave function shown in Fig. 4B is localized on the rings immediately surrounding the dislocation line at the center of the array and is minimally affected by the finite-size effect at the edges of the array. As an artifact of the periodic boundary condition, a second dislocation line with an opposite Burgers vector is present on the boundary of the array. It supports a one-way state in the topological bandgap propagating in the opposite direction, as shown by the blue line in Fig. 4A, with an eigenstate localized around the dislocation center at (0, 6) (Fig. 4C).

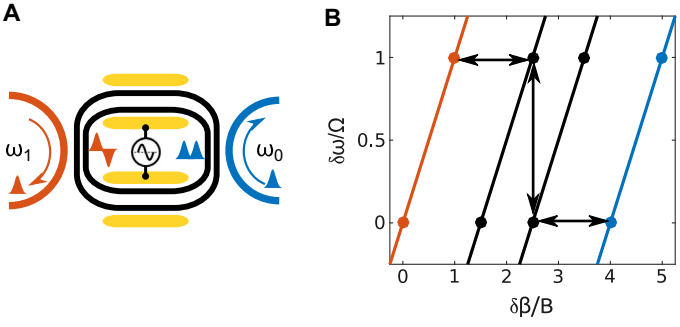


**Fig. 3. Design of the dynamic link ring.** (**A**) Dynamic link ring formed by a slot waveguide. It supports two modes with even and odd transverse profiles, respectively. The yellow pads are radio-frequency modulators that dynamically vary the refractive index of the waveguide. This drives a direct photonic transition between the even and odd modes. The width of the air gap in the slot waveguide at the modulated region is chosen such that the frequency separation between the even and odd modes matches the modulation frequency. At the waveguide coupler to the site rings, this air gap is tapered down to provide phase-matched coupling to the site rings. (**B**) Waveguide dispersion and resonant modes of the site rings and the dynamic link ring. Ω is the free spectral range of the rings, and *B* is the wave vector difference between adjacent resonances in each ring. The orange line corresponds to the dispersion of waveguide mode in the orange site ring and the odd mode in the dynamic link ring at the waveguide coupler region. The blue line corresponds to the dispersion of the waveguide mode in the blue site ring and the even mode in the dynamic link ring at the waveguide coupler region. The black lines correspond to the dispersion of the even and odd waveguide modes of the dynamic link ring at the modulator region. Dots indicate the resonances of each ring. Black arrows show the coupling of a lower frequency mode in the blue site ring to a higher-frequency mode in the orange site ring through a driven transition in the dynamic link ring.

Multimode one-way photonic waveguides can increase the capacity of the unidirectional guiding channel and enable new devices and functionalities (*36*, *37*). In our system, the number of topological modes supported by the dislocation is $\mathbf{G}_v \cdot \mathbf{B}/2\pi$ (*22*, *26*, *30*). A multimode one-way waveguide can be realized in our system by increasing either the amplitude of dislocation or the Chern number. We can double the value of **B** by modulating the dynamic link ring at a frequency 2Ω. Each dynamic link ring then connects states that are two resonances apart in the orange and blue site rings, and we effectively have two interleaved copies of the spiral surface, as shown in Fig. 1D. Each supports a 1D topological state at the dislocation line. This is confirmed by the band diagram shown in Fig. 4C where two pairs of one-way states span the topological bandgap. The wave functions projected onto the $x - y$ plane are similar to Fig. 4 (B and C) for both pairs. Alternatively, one can access a magnetic bandgap with a higher Chern number by choosing a different magnetic flux (*27*, *28*), for example, $\phi = 1/5$ flux quanta. This can be accomplished by changing the spatial gradient of the shifts of the link rings. In this case, the multiple localized states in the topological bandgap have orthogonal spatial wave functions and similar band dispersions.

The topological states localized on the screw dislocation can be experimentally probed by coupling a single-frequency signal, whose frequency detuning δω from the resonance of the rings $\omega_0$ falls within the magnetic bandgap, into one of the site rings around the dislocation through an external waveguide. Here, we numerically simulate what can be probed in such an experiment. We consider an 8 × 8 array of site rings with a single dislocation at the center of the array at (0, 0). A continuous wave input at a frequency detuning $\delta\omega = -0.03\Omega$ from a resonance is coupled into the site ring at (−0.5, 0.5) using an external waveguide. Figure 5 plots the spectral and spatial power distribution of the steady-state solution in the presence of a small loss in the waveguides. Figure 5A shows the static-state power distribution in different frequency sidebands. The input at the $m = 0$ sideband is unidirectionally transported to lower resonance frequencies. Thus, the structure enables one-way frequency conversion. In our simulation, a 5 % round-trip power loss is assumed for each ring; thus, the total power decays while traveling down the frequency axis. To test the robustness of the one-way frequency conversion, we introduce random fluctuations into the resonant frequencies and the inter-ring coupling strengths. We first introduce a random detuning of the resonance frequency $\omega_0$ for each ring. The detuning is drawn from a normal distribution with a mean of 0 and an SD of 0.05Ω, i.e., $\Delta\omega_{0,i}/\Omega \sim \mathcal{N}(0, 0.05)$, where *i* labels individual rings in the array. Figure 5B shows the mean (orange dots) and SD (gray area) of the spectral power distribution averaged over 20 randomly generated configurations. The unidirectionality of the frequency conversion is well preserved. We then introduce a random variation into the

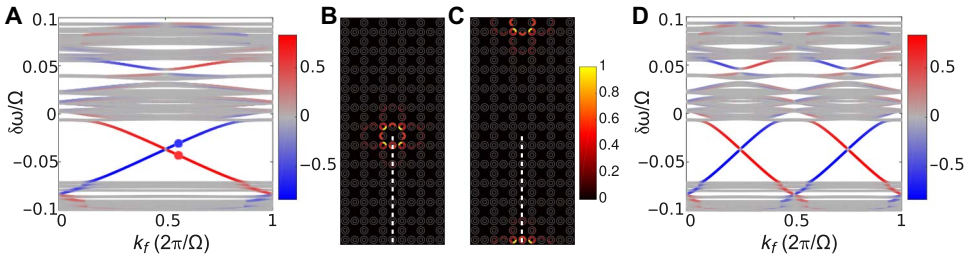


**Fig. 4. 1D topological state trapped by a screw dislocation.** Calculated for the lattice with a screw dislocation shown in Fig. 1, using a 12 × 12 array of site rings. Assume infinite resonant modes along the synthetic frequency dimension and periodic boundary conditions in both the *x* and *y* directions. (**A** and **D**) Band diagram for a lattice with **B** = (0, 0, −1) and **B** = (0, 0, −2), respectively. Color scale represents the difference of eigenstate modal intensity between rings surrounding the dislocation lines centered at (0, 0) and (0, 6). Red lines are one-way states localized on the dislocation centered at (0, 0). Blue lines are one-way states localized on the dislocation centered at (0, 6), as a result of the periodic boundary condition. The red and blue dots represent the states plotted in (B) and (C). (**B** and **C**) Eigenstate intensity distribution. For simplicity, only six columns closest to the center are shown. The dashed line indicates the location of dynamic link rings. For the dynamic link ring, the intensity of the even and odd modes is simply added together for display.

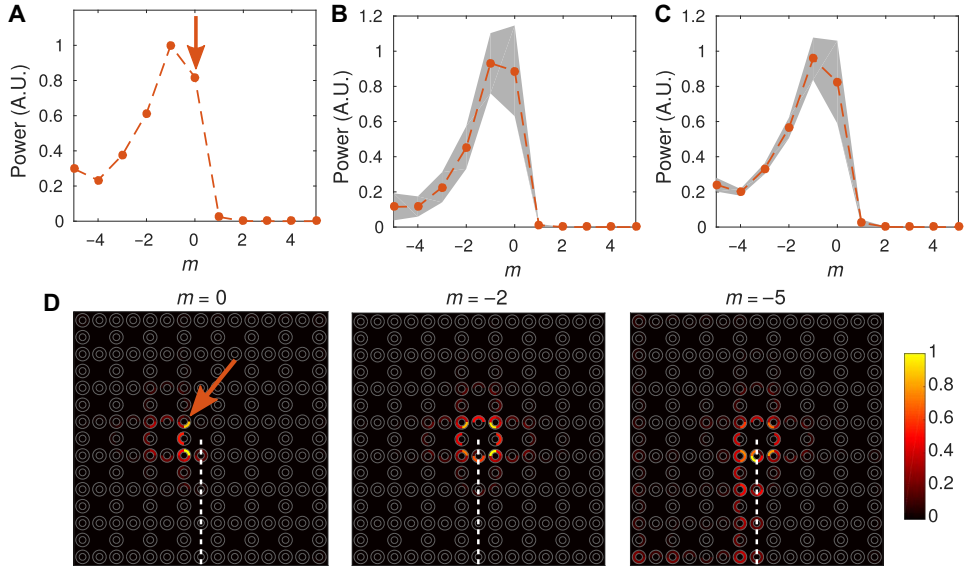


**Fig. 5. Probing the dislocation state.** A screw dislocation is created in an 8 × 8 array of site rings. A single-frequency input is coupled into a site ring at the center through an external waveguide. Eleven sidebands are used, with hard truncation along the frequency boundary (*18*). *m* is the order of sidebands, where *m* = 0 is the input frequency. The input frequency is in the lower magnetic bandgap with a detuning δω = −0.03Ω from the site ring resonance. The orange arrows in (A) and (D) indicate the frequency sideband of the input resonant mode and spatial location of the input ring. (**A**) Steady state aggregated intensity at each sideband. One-way frequency downconversion is observed. (**B**) Adding a normal distributed noise to the resonance of all rings with SD σ = 0.05 for δω/Ω. Orange dots show the mean intensity, and gray areas show the SD. Averaged over 20 configurations. (**C**) Adding a normal distributed noise to the coupling strength between all rings with SD σ = 0.1 for the ratio to the original value. Orange dots show the mean intensity, and gray areas show the SD. Averaged over 20 configurations. A.U., arbitrary units. (**D**) Spatial intensity distribution at three different sidebands. Power is largely localized at the rings immediately surrounding the dislocation line. When the power reaches the bottom edge (*m* = −5), it continues along the branch cut and merges into an edge state of the stripe.

inter-ring coupling strength $\gamma_0$ for each pair of adjacent rings such that $\Delta\gamma_{\langle ij\rangle}/\gamma_0 \sim \mathcal{N}(0, 0.1)$ for each adjacent pair of rings. $\gamma_{\langle ij\rangle} = \Delta\gamma_{\langle ij\rangle} + \gamma_0$ is capped to be within between 0 and 1. The result shown in Fig. 5C again demonstrates the robustness of the one-way frequency conversion. The perturbations we introduce are comparable to the size of the topological bandgap.

Last, we examine the spatial power distribution at different frequency sidebands. As shown in Fig. 5D, the power is concentrated on the rings immediately surrounding the dislocation line and propagates counterclockwise around it. In our simulation, we imposed a hard frequency boundary condition at *m* = ±5 similar to that shown in Fig. 1A. When the signal reaches the bottom frequency layer at *m* = −5, it travels along the branch cut defined by the dynamic link rings and merges into a clockwise edge state at the boundary of the array (Fig. 5D), in agreement with our theoretical analysis. This unrealistic hard cutoff in frequency is added for ease of simulation and is required for experiments aiming to probe the topological states in our system.

In summary, we have shown that existing implementation of 2D topological photonic states based on 2D microring arrays can be readily extended to implement 3D topological insulators. This allows us to study 3D topological effects using an integrated photonic platform, bypassing the difficulty of constructing complex 3D optical

structures. Our proposal also yields a sizable 3D topological bandgap comparable to its 2D counterpart, which provides a clean platform to study the interaction of crystallographic defect with band topology. As an example, our system can be used to demonstrate a robust unidirectional 1D waveguide pinned by a screw dislocation in a 3D TI, which performs one-way frequency conversion for the input signal. The dislocation is implemented through dynamically modulating a few microrings, substantially reducing the experimental challenge for studying lattice and band topology in the synthetic frequency dimension.

## MATERIALS AND METHODS

The numerical calculation of band structures and wave functions in this work used the transfer matrix method, which accounts for waveguide modal amplitudes at different parts of each ring. Here, we provide a brief summary of the transfer matrix method. A more detailed account is presented in the Supplementary Materials.

The electric field $E$ inside the waveguide forming a ring can be written as

$$E(t, r_\perp, z) = \sum_m \mathcal{E}_m(t, z) E_m(r_\perp) e^{-i(\omega_m + \delta\omega)t}$$

Here, $r_\perp$ and $z$ represent the transverse and propagation directions in the ring, respectively, and $t$ represents time. $E(r_\perp)$ is the transverse modal profile in the waveguide. $\omega_m$ and $\mathcal{E}_m(t, z)$ are the resonant frequency and the modal amplitude of the $m$th sideband, respectively. $\delta\omega$ is a small frequency detuning from the resonance.

In a continuous section of the waveguide, in the absence of any modulators or couplers, the steady-state solution of the modal amplitude $\mathcal{E}_m(t, z)$ is

$$\mathcal{E}_m(z) = \mathcal{E}_m(z_0) e^{i\beta(\omega_m + \delta\omega)\cdot(z - z_0)} \quad (6)$$

where $\beta(\omega_m + \delta\omega)$ is the wave vector of the waveguide mode at the frequency $\omega_m + \delta\omega$. When the waveguide dispersion is nearly linear with a frequency-independent group velocity of $v_g$, $\beta(\omega_m + \delta\omega)$ is linear with respect to $m$ and $\delta\omega$, i.e., $\beta(\omega_m + \delta\omega) \approx \beta(\omega_0) + (m\Omega + \delta\omega)/v_g$.

A waveguide coupler between the site ring and the link ring in our system, as shown in fig. S1, was characterized by a 2 × 2 scattering matrix relating the two input waveguide modes to two output waveguide modes

$$\begin{pmatrix} \mathcal{E}_m^{1,\text{out}} \\ \mathcal{E}_m^{2,\text{out}} \end{pmatrix} = \begin{pmatrix} r & i\gamma \\ i\gamma & r \end{pmatrix} \begin{pmatrix} \mathcal{E}_m^{1,\text{in}} \\ \mathcal{E}_m^{2,\text{in}} \end{pmatrix} \quad (7)$$

Here, the indices 1 and 2 represent two waveguides that belong to two rings. $\gamma$ represents the inter-waveguide coupling, and $\sqrt{\gamma^2 + r^2} = 1$ owing to energy conservation.

Similarly, a modulator in the dynamic link ring was characterized by a scattering matrix connecting the different frequency sidebands at the input and output. For a generic modulator, this scattering matrix may have very high dimensions since multiple frequency sidebands can be generated from a single-frequency input. However, for the specific modulator design shown in Fig. 3 and fig. S1, mode conversion only occurs between a lower-frequency even mode and a higher-frequency odd mode with the same wave vector. Thus, this modulator was characterized by a 2 × 2 scattering matrix

$$\begin{pmatrix} \mathcal{E}_m^{\text{even,out}} \\ \mathcal{E}_{m+1}^{\text{odd,out}} \end{pmatrix} = \begin{pmatrix} \cos C & i\sin C \\ i\sin C & \cos C \end{pmatrix} \begin{pmatrix} \mathcal{E}_m^{\text{even,in}} \\ \mathcal{E}_{m+1}^{\text{odd,in}} \end{pmatrix} \quad (8)$$

Here, $C$ represents the coupling between the two modes and is proportional to the strength of the refractive index modulation.

The set of modal amplitudes $\mathcal{E}_m$ in the microring array is related by a set of linear equations based on Eqs. 6 to 8. With the proper choice of the reference point $z_0$ in Eq. 6 in each waveguide section, the system of equations can be shown to have the form

$$\bar{\mathcal{E}} = e^{i\delta\omega \cdot T/4} S \cdot \bar{\mathcal{E}} \quad (9)$$

where $\bar{\mathcal{E}}$ is a vector of all the independent modal amplitudes in the microring arrays. $T$ is the round-trip time in the microring. The factor of 1/4 enters because each site ring is separated into four continuous sections of waveguide by the waveguide couplers to the linkrings. The scattering matrix $S$ captures the different device geometries and modulation configurations. The eigenfrequency $\delta\omega$ and eigenstates $\bar{\mathcal{E}}$ of the system can be obtained by solving the eigenvalue problem of the scattering matrix $S$. The results presented in Figs. 2 and 4 were obtained this way.

When the system is coupled to external waveguides, the external input results in an additional inhomogeneous term $\bar{\mathcal{B}}$ to Eq. 9

$$\bar{\mathcal{E}} = e^{i\delta\omega \cdot T/4} S \cdot \bar{\mathcal{E}} + \bar{\mathcal{B}}$$

where $S$ is also modified to include the coupling to external waveguides as the photons go through round trips in the ring. Thus, $S$ incorporates loss of photons due to external coupling. The steady-state solution $\bar{\mathcal{E}}$ can be calculated as

$$\bar{\mathcal{E}} = (I - e^{i\delta\omega \cdot T/4} S)^{-1} \bar{\mathcal{B}}$$

where $I$ is an identity matrix. The results presented in Fig. 5 was obtained this way.

## SUPPLEMENTARY MATERIALS

Supplementary material for this article is available at http://advances.sciencemag.org/cgi/content/full/4/10/eaat2774/DC1

Section S1. Floquet interpretation of the tight-binding Hamiltonian
Section S2. Transfer-matrix method for the microring array
Section S3. Designing the coupling and modulation strength of the link ring
Section S4. Waveguide coupler and modulator design
Fig. S1. Modal amplitudes used in the transfer matrix method.
Fig. S2. Effective scattering matrix parameters for the static and dynamic link rings.
Fig. S3. Dynamic link ring modulator and coupler design.
Fig. S4. Static link ring coupler design.
Table S1. A sample device design.
References (*38*–*41*)

## REFERENCES AND NOTES

1. F. D. M. Haldane, S. Raghu, Possible realization of directional optical waveguides in photonic crystals with broken time-reversal symmetry. *Phys. Rev. Lett.* **100**, 013904 (2008).

2. Z. Wang, Y. Chong, J. D. Joannopoulos, M. Soljačić, Observation of unidirectional backscattering-immune topological electromagnetic states. *Nature* **461**, 772–775 (2009).
3. R. O. Umucalılar, I. Carusotto, Artificial gauge field for photons in coupled cavity arrays. *Phys. Rev. A* **84**, 043804 (2011).
4. M. Hafezi, E. A. Demler, M. D. Lukin, J. M. Taylor, Robust optical delay lines with topological protection. *Nat. Phys.* **7**, 907–912 (2011).
5. K. Fang, Z. Yu, S. Fan, Realizing effective magnetic field for photons by controlling the phase of dynamic modulation. *Nat. Photonics* **6**, 782–787 (2012).
6. M. C. Rechtsman, J. M. Zeuner, Y. Plotnik, Y. Lumer, D. Podolsky, F. Dreisow, S. Nolte, M. Segev, A. Szameit, Photonic Floquet topological insulators. *Nature* **496**, 196–200 (2013).
7. M. Hafezi, S. Mittal, J. Fan, A. Migdall, J. M. Taylor, Imaging topological edge states in silicon photonics. *Nat. Photonics* **7**, 1001–1005 (2013).
8. A. B. Khanikaev, S. H. Mousavi, W.-K. Tse, M. Kargarian, A. H. MacDonald, G. Shvets, Photonic topological insulators. *Nat. Mater.* **12**, 233–239 (2013).
9. G. Q. Liang, Y. D. Chong, Optical resonator analog of a two-dimensional topological insulator. *Phys. Rev. Lett.* **110**, 203904 (2013).
10. M. Pasek, Y. D. Chong, Network models of photonic Floquet topological insulators. *Phys. Rev. B* **89**, 075113 (2014).
11. W.-J. Chen, S.-J. Jiang, X.-D. Chen, B. Zhu, L. Zhou, J.-W. Dong, C. T. Chan, Experimental realization of photonic topological insulator in a uniaxial metacrystal waveguide. *Nat. Commun.* **5**, 5782 (2014).
12. T. Ma, A. B. Khanikaev, S. H. Mousavi, G. Shvets, Guiding electromagnetic waves around sharp corners: Topologically protected photonic transport in metawaveguides. *Phys. Rev. Lett.* **114**, 127401 (2015).
13. X. Cheng, C. Jouvaud, X. Ni, S. Hossein Mousavi, A. Z. Genack, A. B. Khanikaev, Robust reconfigurable electromagnetic pathways within a photonic topological insulator. *Nat. Mater.* **15**, 542–548 (2016).
14. X.-L. Qi, S.-C. Zhang, Topological insulators and superconductors. *Rev. Mod. Phys.* **83**, 1057–1110 (2011).
15. M. Z. Hasan, C. L. Kane, *Colloquium*: Topological insulators. *Rev. Mod. Phys.* **82**, 3045–3067 (2010).
16. L. Lu, C. Fang, L. Fu, S. G. Johnson, J. D. Joannopoulos, M. Soljačić, Symmetry-protected topological photonic crystal in three dimensions. *Nat. Phys.* **12**, 337–340 (2016).
17. A. Slobozhanyuk, S. H. Mousavi, X. Ni, D. Smirnova, Y. S. Kivshar, A. B. Khanikaev, Three-dimensional all-dielectric photonic topological insulator. *Nat. Photonics* **11**, 130–136 (2017).
18. L. Yuan, Y. Shi, S. Fan, Photonic gauge potential in a system with a synthetic frequency dimension. *Opt. Lett.* **41**, 741–744 (2016).
19. Q. Lin, M. Xiao, L. Yuan, S. Fan, Photonic Weyl point in a two-dimensional resonator lattice with a synthetic frequency dimension. *Nat. Commun.* **7**, 13731 (2016).
20. M. Minkov, V. Savona, Haldane quantum Hall effect for light in a dynamically modulated array of resonators. *Optica* **3**, 200–206 (2016).
21. T. Ozawa, H. M. Price, N. Goldman, O. Zilberberg, I. Carusotto, Synthetic dimensions in integrated photonics: From optical isolation to four-dimensional quantum Hall physics. *Phys. Rev. A* **93**, 043827 (2016).
22. Y. Ran, Y. Zhang, A. Vishwanath, One-dimensional topologically protected modes in topological insulators with lattice dislocations. *Nat. Phys.* **5**, 298–303 (2009).
23. L. Fu, C. L. Kane, E. J. Mele, Topological insulators in three dimensions. *Phys. Rev. Lett.* **98**, 106803 (2007).
24. Z. Ringel, Y. E. Kraus, A. Stern, Strong side of weak topological insulators. *Phys. Rev. B* **86**, 045102 (2012).
25. J. M. Kosterlitz, D. J. Thouless, Ordering, metastability and phase transitions in two-dimensional systems. *J. Phys. C Solid State Phys.* **6**, 1181 (1973).
26. L. Lu, Z. Wang, Topological one-way fiber of second Chern number. arXiv:1611.01998 (2016).
27. D. J. Thouless, M. Kohmoto, M. P. Nightingale, M. den Nijs, Quantized Hall conductance in a two-dimensional periodic potential. *Phys. Rev. Lett.* **49**, 405–408 (1982).
28. D. Osadchy, J. E. Avron, Hofstadter butterfly as quantum phase diagram. *J. Math. Phys.* **42**, 5665–5671 (2001).
29. J. C. Y. Teo, C. L. Kane, Topological defects and gapless modes in insulators and superconductors. *Phys. Rev. B* **82**, 115120 (2010).
30. R. Bi, Z. Yan, L. Lu, Z. Wang, Topological defects in Floquet systems: Anomalous chiral modes and topological invariant. *Phys. Rev. B* **95**, 161115 (2017).
31. K. Kawamura, A new theory on scattering of electrons due to spiral dislocations. *Z. Phys. B* **29**, 101–106 (1978).
32. D. M. Bird, A. R. Preston, Observation of Berry's geometrical phase in electron diffraction from a screw dislocation. *Phys. Rev. Lett.* **61**, 2863–2866 (1988).
33. R. Bausch, R. Schmitz, Ł. A. Turski, Single-particle quantum states in a crystal with topological defects. *Phys. Rev. Lett.* **80**, 2257–2260 (1998).
34. K. Fang, Z. Yu, S. Fan, Photonic Aharonov-Bohm effect based on dynamic modulation. *Phys. Rev. Lett.* **108**, 153901 (2012).
35. L. D. Tzuang, K. Fang, P. Nussenzveig, S. Fan, M. Lipson, Non-reciprocal phase shift induced by an effective magnetic flux for light. *Nat. Photonics* **8**, 701–705 (2014).
36. S. A. Skirlo, L. Lu, M. Soljačić, Multimode one-way waveguides of large chern numbers. *Phys. Rev. Lett.* **113**, 113904 (2014).
37. D. Wang, C. Qiu, P. T. Rakich, Z. Wang, Guide-wave photonic pulling force using one-way photonic chiral edge states, in *2015 Conference on Lasers and Electro-Optics (CLEO: 2015)* (Optical Society of America, 2015), p. FM2D.7.
38. T. Kitagawa, E. Berg, M. Rudner, E. Demler, Topological characterization of periodically driven quantum systems. *Phys. Rev. B* **82**, 235114 (2010).
39. M. S. Rudner, N. H. Lindner, E. Berg, M. Levin, Anomalous edge states and the bulk-edge correspondence for periodically driven two-dimensional systems. *Phys. Rev. X* **3**, 031005 (2013).
40. Y. Shi, W. Shin, S. Fan, Multi-frequency finite-difference frequency-domain algorithm for active nanophotonic device simulations. *Optica* **3**, 1256–1259 (2016).
41. X. Xiao, H. Xu, X. Li, Z. Li, T. Chu, Y. Yu, J. Yu, High-speed, low-loss silicon Mach–Zehnder modulators with doping optimization. *Opt. Express* **21**, 4116–4125 (2013).



**Acknowledgments**

**Funding:** This work was supported by U.S. Air Force of Scientific Research grant no. FA9550-17-1-0002 and U.S. NSF grant no. CBET-1641069. Q.L. acknowledges the support of a Stanford Graduate Fellowship. X.-Q.S. and S.-C.Z. acknowledge support from the U.S. Department of Energy, Office of Basic Energy Sciences under contract DE-AC02-76SF00515. **Author contributions:** Q.L., X.-Q.S., and S.F. conceived the idea of constructing a 3D photonic topological insulator in a ring resonator lattice. Q.L., X.-Q.S., and M.X. conceived the scheme for realizing a screw dislocation. Q.L. performed the numerical studies. All authors contributed to the discussion of the results and writing of the manuscript. S.F. supervised the project. **Competing interests:** The authors declare that they have no competing interests. **Data and materials availability:** All data needed to evaluate the conclusions in the paper are present in the paper and/or the Supplementary Materials. Additional data related to this paper may be requested from the authors.

Submitted 9 February 2018
Accepted 10 September 2018
Published 19 October 2018
10.1126/sciadv.aat2774

**Citation:** Q. Lin, X.-Q. Sun, M. Xiao, S.-C. Zhang, S. Fan, A three-dimensional photonic topological insulator using a two-dimensional ring resonator lattice with a synthetic frequency dimension. *Sci. Adv.* **4**, eaat2774 (2018).

ScienceAdvances

# A three-dimensional photonic topological insulator using a two-dimensional ring resonator lattice with a synthetic frequency dimension

Qian Lin, Xiao-Qi Sun, Meng Xiao, Shou-Cheng Zhang and Shanhui Fan

*Sci Adv* **4** (10), eaat2774.
DOI: 10.1126/sciadv.aat2774